

Effects of overlap uniformness for ptychography

Xiaojing Huang¹, Hanfei Yang¹, Ross Harder², Yeukuang Hwu³,
Ian K. Robinson^{4,5}, and Yong S. Chu¹

¹National Synchrotron Light Source II, Brookhaven National Laboratory, Upton, NY 11973, USA

²Advanced Photon Source, Argonne National Laboratory, Argonne, IL 60439, USA

³Institute of Physics, Academia Sinica, Taipei, 11529, Taiwan

⁴London Centre for Nanotechnology, University College London, London, WC1H 0AH, UK

⁵Research Complex at Harwell, Didcot, Oxfordshire OX11 0DE, UK

Abstract: We propose to conduct ptychography scans following the Fermat spiral trajectory, which provides more uniform coverage and higher overlapping ratio with the same number of scan points over the same area. Numerical simulations show that the reconstructed image quality is improved by at least 4% with Fermat spiral compared with the image using the concentric scan pattern. A more significant performance enhancement was observed from experimental data. These results confirm that the Fermat spiral pattern increases image quality and reconstruction tolerance on data with imperfections, especially for low overlapping conditions.

© 2014 Optical Society of America

OCIS codes: (340.0340) X-ray optics; (100.5070) Phase retrieval; (110.3010) Image reconstruction techniques

References and links

1. R. Hegerl and W. Hoppe, "Dynamic theory of crystalline structure analysis by electron diffraction in inhomogeneous primary wave field," *Ber. Bunsenges. Phys. Chem.* **74**, 1148 (1970).
2. J. Rodenburg, A. Hurst, A. Cullis, B. Dobson, F. Pfeiffer, O. Bunk, C. David, K. Jefimovs, and I. Johnson, "Hard-X-Ray Lensless Imaging of Extended Objects," *Physical Review Letters* **98**, 034,801 (2007).
3. P. Thibault, M. Dierolf, A. Menzel, O. Bunk, C. David, and F. Pfeiffer, "High-resolution scanning x-ray diffraction microscopy," *Science* **321**, 379–382 (2008).
4. M. Guizar-Sicairos and J. Fienup, "Phase retrieval with transverse translation diversity: a nonlinear optimization approach," *Optics Express* **16**(10), 7264–7272 (2008).
5. A. Maiden and J. Rodenburg, "An improved ptychographical phase retrieval algorithm for diffractive imaging," *Ultramicroscopy* **109**, 1256–1262 (2009).
6. P. Thibault and M. Guizar-Sicairos, "Maximum-likelihood refinement for coherent diffractive imaging," *New Journal of Physics* **14**, 063,004 (2012).
7. A. Maiden, M. Humphry, M. Sarahan, B. Kraus, and J. Rodenburg, "An annealing algorithm to correct positioning errors in ptychography," *Ultramicroscopy* **120**, 64–72 (2012).
8. M. Beckers, T. Senkbeil, T. Gorniak, K. Giewekemeyer, T. Salditt, and A. Rosenhahn, "Drift correction in ptychographic diffractive imaging," *Ultramicroscopy* **126**, 44–47 (2013).
9. F. Zhang, I. Peterson, J. Vila-Comamala, A. Diaz, F. Berenguer, R. Bean, B. Chen, A. Menzel, I. Robinson, and J. Rodenburg, "Translation position determination in ptychographic coherent diffraction imaging," *Optics Express* **21**(11), 13,592–13,606 (2013).
10. O. Bunk, M. Dierolf, S. Kynde, I. Johnson, O. Marti, and F. Pfeiffer, "Influence of the overlap parameter on the convergence of the ptychographical iterative engine," *Ultramicroscopy* **108**, 481–487 (2008).
11. P. Thibault, M. Dierolf, O. Bunk, A. Menzel, and F. Pfeiffer, "Probe retrieval in ptychographic coherent diffractive imaging," *Ultramicroscopy* **109**, 338–343 (2009).
12. M. Dierolf, P. Thibault, A. Menzel, C. Kewish, K. Jefimovs, I. Schlichting, K. Kong, O. Bunk, and F. Pfeiffer, "Ptychographic coherent diffractive imaging of weakly scattering specimens," *New Journal of Physics* **12**, 035,017 (2010).

13. C. Kewish, P. Thibault, M. Dierolf, O. Bunk, A. Menzel, J. Vila-Comamala, K. Jefimovs, and F. Pfeiffer, "Ptychographic characterization of the wavefield in the focus of reflective hard X-ray optics," *Ultramicroscopy* **110**, 325–329 (2010).
14. M. Dierolf, A. Menzel, P. Thibault, P. Schneider, C. Kewish, R. Wepf, O. Bunk, and F. Pfeiffer, "Ptychographic X-ray computed tomography at the nanoscale," *Nature* **467**, 436–440 (2010).
15. P. Thibault and A. Menzel, "Reconstructing state mixtures from diffraction measurements," *Nature* **494**, 68–71 (2013).
16. X. Huang, H. Yan, E. Nazaretski, R. Conley, N. Bouet, J. Zhou, K. Lauer, L. Li, D. Eom, D. Legnini, R. Harder, I. Robinson, and Y. Chu, "11 nm hard X-ray focus from a large-aperture multilayer Laue lens," *Scientific Reports* **3**, 3562 (2013).
17. H. Vogel, "A better way to construct the sunflower head," *Mathematical Biosciences* **44**, 179–189 (1979).
18. H. Huntley, *The Divine Proportion* (Dover Publications, Inc., New York, 1970).
19. E. Lockwood, *A Book of Curves* (Cambridge University Press, Cambridge, 1967).
20. J. Miao, Y. Nishino, Y. Kohmura, B. Johnson, C. Song, S. Risbud, and T. Ishikawa, "Quantitative image reconstruction of GaN quantum dots from oversampled diffraction intensities alone," *Physical Review Letters* **95**, 085,503 (2005).
21. X. Huang, H. Miao, J. Steinbrener, J. Nelson, A. Stewart, D. Shapiro, and C. Jacobsen, "Signal to noise considerations in diffraction and conventional microscopy," *Optics Express* **17**(16), 13,541–13,553 (2009).
22. X. Huang, M. Wojcik, N. Burdet, I. Peterson, G. Morrison, D. Vine, D. Legnini, R. Harder, Y. Chu, and I. K. Robinson, "Quantitative X-ray wavefront measurements of Fresnel zone plate and K-B mirrors using phase retrieval," *Optics Express* **20**(21), 24,038–24,048 (2012).
23. R. Wilke, M. Vassholz, and T. Salditt, "Semi-transparent central stop in high-resolution X-ray ptychography using Kirkpatrick-Baez focusing," *Acta Crystallographica* **A69**, 490–497 (2013).
24. N. Metropolis, A. Rosenbluth, M. Rosenbluth, A. Teller, and E. Teller, "Equations of state calculations by fast computing machines," *Journal of Chemical Physics* **21**, 1087–1092 (1953).
25. W. Press, S. Teukolsky, W. Vetterling, and B. Flannery, *Numerical Recipes in C*, 2nd ed. (Cambridge University Press, Cambridge, 2002).

1. Introduction

Originated for electron microscopy [1] and emerging as a powerful X-ray imaging technique [2], ptychography has been experiencing rapid developments of improving image quality, enhancing reliability and extending its applications to a variety of scientific problems. Ptychography relies on the information recorded in the far-field diffraction patterns when the sample is scanned through a confined coherent X-ray illumination. To lead a successful reconstruction, it is crucial to have sufficient overlapping between adjacent scan spots, so that the same subset of the sample is exposed multiple times, which ensures the oversampling condition for phase-retrieval. With *a priori* knowledge of scanning positions, ptychography alleviates convergence difficulty and is capable to recover both the transmission function of the sample and the wavefront of the incident X-ray beam [3, 4, 5, 6].

Recently developed position-correction mechanisms [4, 7, 8, 9] even relax the accuracy requirement on the scanning positions. Nevertheless, the scan pattern layout plays the critical role in determining the performance of ptychography, because it defines the sampling ratio and overlapping uniformness. It is suggested an optimum overlap value of 60%, which minimizes the necessary radiation dose without sacrificing image quality [10]. It has also been pointed out that the periodicity in a mesh scan (as shown in Fig. 1(a)) will cause "raster grid pathology", which introduces periodic artifacts in the reconstructed images [11]. A scan pattern with concentric trajectory shown in Fig. 1(b) was proposed to eliminate translational symmetry [12], and thus remove the aforementioned artifact. The concentric scan pattern has been widely used and delivers high quality images in various applications [13, 14, 15, 16].

Generally, an ideal scan pattern for ptychography would expect to have two desired features: lack of symmetry and uniform coverage (*i.e.* overlap). In this paper, we propose the use of Fermat spiral pattern as a promising scan trajectory that fulfills these two demanding properties. The superb performance is verified through numerical simulation and experimental measurement. The results indicate that the Fermat spiral is more robust, especially for relatively low

overlapping conditions.

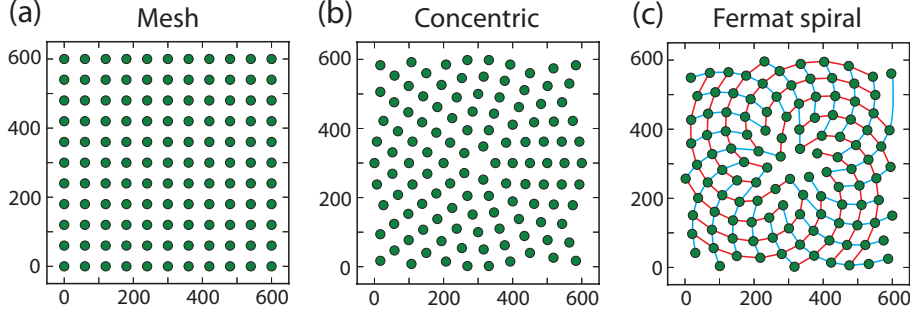


Fig. 1. Scan positions for ptychograph: (a) 11×11 mesh pattern with 121 points, (b) concentric pattern with 5 points in the first ring, 50 pixel radial increment step and 119 points in total, (c) Fermat spiral pattern with 31 pixel increment and 119 points in total, which contains two sets of equiangular spirals: 13 clockwise (red curves) and 21 counterclockwise (blue curves). It is noticeable that 13 and 21 are two consecutive Fibonacci numbers.

2. Fermat spiral

Space optimization appears in many biological systems, such as the arrangements of branches and leaves on the stems of plants for even reception of sunlight, the floret patterning of sunflowers for equal exposure to pollinators. Inspired by these hints represented in Nature, an elegant analytic expression was proposed to construct the tightly packed sunflower seeds [17]. In polar coordinates (r, θ) , it has the form

$$r = c\sqrt{n}, \theta = n\phi_0, \quad (1)$$

where c is a constant scaling factor for the radius, n is the index number of the seed, and ϕ_0 is the divergence angle $\sim 137.508^\circ$.

The angle 137.508° is known as the golden angle, which divides a circle in the golden ratio ϕ , $(1 + \sqrt{5})/2$ or 1.618. A rational derivation for this angle is given in [17], where the branch arrangement is optimized to be evenly spaced. Denoting branch angular increment as p/q , which stands for q branches making p complete turns around the stem, it is shown that to ensure all branches sharing the same spatial relationship and fitting into the largest existing gap, p and q have to be two adjacent Fibonacci number of even order (F_{2v} and F_{2v+2}). With the limit that the number of branches goes to infinity, the optimal angular stepsize p/q becomes $\lim_{v \rightarrow \infty} (F_{2v}/F_{2v+2}) = \lim_{v \rightarrow \infty} [(F_{2v}/F_{2v+1})(F_{2v+1}/F_{2v+2})] = 1/\phi^2$ [18], so that the corresponding divergence angle is $\phi_0 = 2\pi/\phi^2 \approx 137.508^\circ$.

An intuitive reason for the square root relationship between radius and index number arises from the requirement that each seed takes equal area. Assuming that n seeds occupy a circular area with radius r , the space occupied by each seed is expected to be a constant, or $\pi r^2 \propto n$, so that the radius r is proportional to \sqrt{n} .

Combining equations in Eq. 1, the proposed pattern takes the form $r^2 = c^2/\phi_0 \cdot \theta$. This is an expression for a parabolic spiral ($r^2 = \alpha\theta$), which was first discussed by P. Fermat in 1636 and named after him [19].

Fig.1(c) shows a Fermat spiral pattern that is constructed with $c = 31$ pixels and spreads over a 600 pixel \times 600 pixel area. The radius scaling factor c is tuned to make sure that the total number of points matches with that of the concentric pattern over the same area as shown in Fig.1(b). The Fermat spiral pattern indeed depicts the capitulum of a sunflower. The points

are located at the intersections of two sets of equiangular spirals: 13 clockwise and 21 counterclockwise, indicated as the red and blue curves in Fig.1(c) respectively. This pattern is uniformly distributed and has neither periodicity nor noticeable symmetry, which perfectly fulfills requirements for ptychography measurement.

3. Simulation result

The performance of the Fermat spiral as a scan pattern for ptychography is tested with a numerical simulation. Fig. 2 shows the simulated complex object and probe. All three scan patterns shown in Fig. 1 are evaluated. They cover the same 600×600 pixel area, and the total number of points are almost equivalent, 121, 119 and 119, respectively. Perfect condition is assumed with no noise, no missing pixels and no positioning inaccuracy. The ptychography reconstructions are performed with the Difference Map algorithm [3]. Each reconstruction cycle takes 1000 iteration, with the last 200 iteration outputs averaged to give the final images. The reconstruction was repeated 10 times with individual random guesses of both the object and probe.

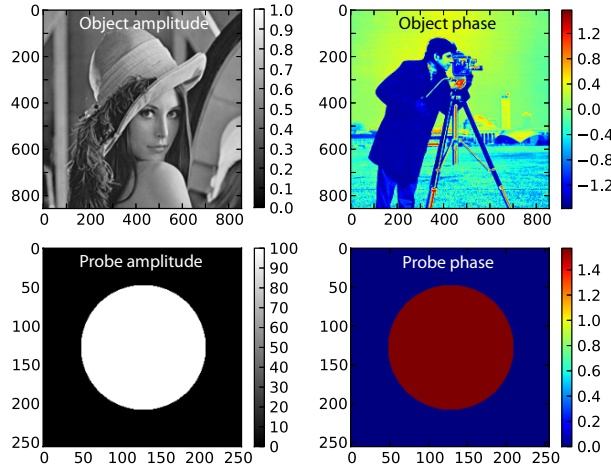


Fig. 2. Top row: amplitude and phase of the simulated object. Bottom row: amplitude and phase of the simulated illumination with a disk shape.

The reconstructed amplitude and phase images are shown in Fig. 3 and Fig. 4, respectively. The “raster grid pathology” is clearly observed in the reconstructed amplitude and phase images with the mesh pattern. Because the scanning points are exactly located at regular grids in this ideally controlled simulation, this pathology effect is magnified. Both the concentric and Fermat spiral scans eliminate the periodic artifact. Two criteria are used to evaluate the obtained image quality: the real-space R factor [20] which measures the difference between the initial image intensity I_0 and the reconstructed image intensity I_{recon} , and the signal-to-noise ratio SNR estimated from correlation coefficient r_{cc} [21] which represents the similarity between reconstructed images from individual random starts. R and SNR are calculated as following:

$$R = \sqrt{\frac{\sum (I_0 - I_{recon})^2}{\sum (I_0 + I_{recon})^2}}, \quad (2)$$

$$SNR = \sqrt{\frac{r_{cc}}{1 - r_{cc}}}, r_{cc} = \frac{\sum (I_{recon1} - \bar{I}_{recon1})(I_{recon2} - \bar{I}_{recon2})}{\sqrt{\sum (I_{recon1} - \bar{I}_{recon1})^2 \sum (I_{recon2} - \bar{I}_{recon2})^2}}. \quad (3)$$

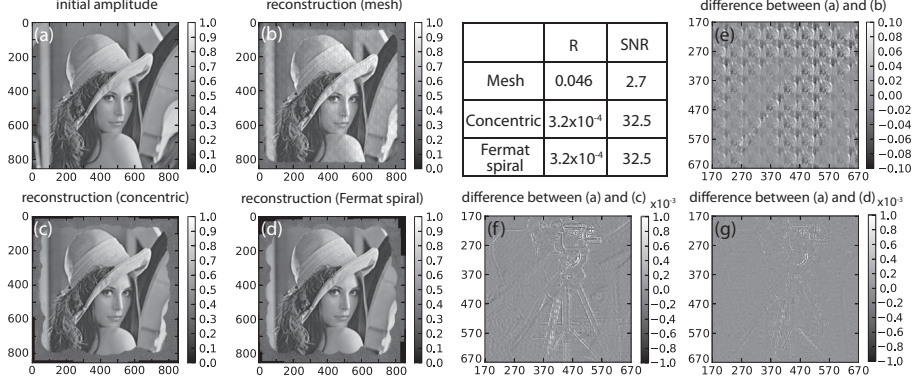


Fig. 3. (a) The initial object amplitude. The reconstructed amplitude using mesh pattern (b), concentric pattern (c) and Fermat spiral pattern (d). (e)(f)(g) are difference images between the initial amplitude and reconstructed amplitudes.

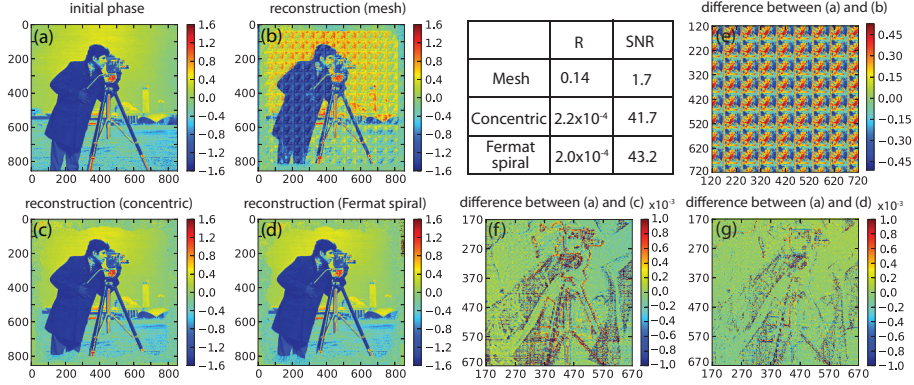


Fig. 4. (a) The initial object phase. The reconstructed phase using mesh pattern (b), concentric pattern (c) and Fermat spiral pattern (d). (e)(f)(g) are difference images between the initial phase and reconstructed phases.

A higher quality image features a lower R value and a higher SNR value. The reconstructed phase part is evaluated using the same methods, but replacing intensity I with phase ϕ .

The central region with 500×500 pixels are used to calculate those criteria. For each scan pattern, 10 R values and 45 SNR values (C_{10}^2) of both intensity and phase are estimated from 10 reconstructions. The averaged values are summarized in the inset tables of Fig. 3 and Fig. 4. For the recovered amplitude, the concentric pattern and the Fermat spiral give images with the same quality. While, the Fermat spiral provides slightly better phase image with improvements of 10% in R and 4% in SNR , respectively.

To better understand this improvement in image quality with the Fermat spiral pattern, the overlap maps of all those 3 tested scan patterns are generated by assigning pixels inside the probe disk to 1, outside pixels to zero and accumulating counts with multiple exposures. The obtained overlap maps are shown in the top row of Fig. 5, which reserve the major features in the scan patterns as shown in Fig. 1. The overlapping ratio is estimated as

$$\sigma = \frac{\sum_{j=1}^{N-1} |P(r-r_j)| |P(r-r_{j+1})|}{\sum_{j=1}^{N-1} |P(r-r_j)|^2}, \quad (4)$$

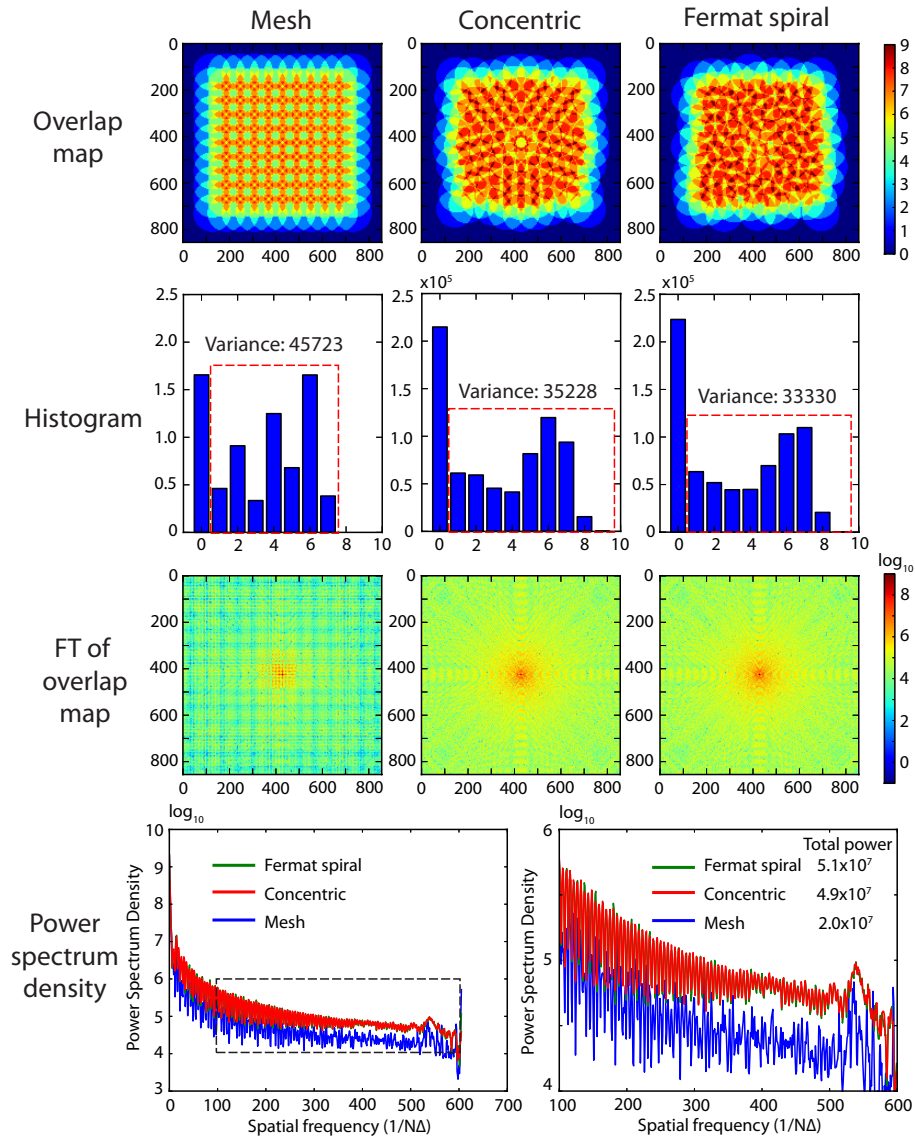


Fig. 5. Top row: the overlap maps for mesh, concentric and Fermat spiral patterns. Second row: histograms of pixel values in the overlap maps. Third row: Fourier transfer of the overlap maps. Bottom row: power spectrum density curve of the third row.

where r_j stands for the translation vector for j th scan point. In the simulated condition, the probe has a disk shape with 80 pixel radius, the overlapping ratios for the mesh, concentric and Fermat spiral patterns are 52.9%, 53.7% and 54.5%, respectively. Since the Fermat spiral only increases overlapping ratio by about 1% compared with the concentric pattern, other aspects should contribute to the improvement of image quality. When plot the histogram of the counts in the overlap map (the second row in Fig. 5), the count variances for pixels exposed at least once are 45723, 35228 and 33330 for mesh, concentric and Fermat spiral patterns, respectively. It implies that the Fermat spiral scan does the best to distribute coverage evenly to different overlap levels. On the other hand, the overlap uniformness can be studied through the Fourier transfer of the overlap maps (shown in the third row of Fig. 5) by checking how the power spectrum density extends to different spatial frequency regions. Plots in the bottom row of Fig. 5 show that the concentric and Fermat spiral patterns distribute 2.5 times more power to high spatial frequency compared with mesh pattern, and the Fermat spiral is about 4% higher than the concentric pattern. This is an evidence for that the Fermat spiral pattern indeed represents more randomly arranged points and provides more uniform coverage.

4. Experimental results

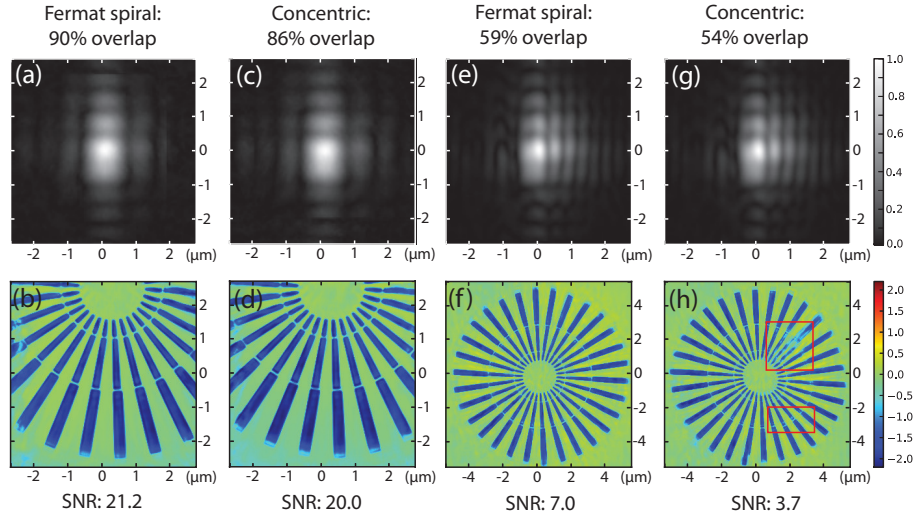


Fig. 6. Top row: the overlap maps for mesh, concentric and Fermat spiral patterns. Second row: histograms of pixel values in the overlap maps. Third row: Fourier transfer of the overlap maps. Bottom row: power spectrum density curve of the third row.

The performances of concentric and Fermat spiral patterns were compared through X-ray experiment data. The measurement was conducted at Beamline 34-ID-C, Advanced Photon Source of Argonne National Laboratory. The instrument setup is similar to previously reported experiment [22]. Coherent 9.6 keV X-rays were focused by K-B mirrors down to about $1 \mu\text{m}$. A star pattern made of $1.2 \mu\text{m}$ thick gold was placed near the focal plane. A Timepix detector with $55 \mu\text{m}$ pixel size recorded far-field diffraction patterns at 2 meter away from the test pattern. To increase the dynamic range of the measurement, a $1.5 \times 1.5 \text{ mm}$ silicon square with $275 \mu\text{m}$ thickness was used to attenuate about 90% of the central part ($\sim 27 \times 27$ pixels) of the diffraction pattern [23]. Each scan position accumulates 15 exposures with 1 second illumination time. A data array of 224×224 pixels was cropped out for reconstruction, which determines the real-space pixel size of 21 nm.

Ptychography scan data were collected in two overlapping conditions. For the concentric pattern, the highly overlapping measurement scans over a $4 \times 4 \mu\text{m}$ area with a radical increment step of 200 nm. The less overlapped scan covers a $12 \times 12 \mu\text{m}$ area with 600 nm radical increment step. The overlapping ratios are 86% and 54%, respectively. For the Fermat spiral pattern, the scanning areas cover the same ranges, and the scaling constants are chosen to be 126 nm and 377 nm, respectively, to give the same number of measurement points as in the corresponding concentric scans. The corresponding overlapping ratios are 90% and 59%, respectively. All scans consist of 323 positions.

The same reconstruction approach as used in the simulation was used to recover images from the experimental data. The obtained probe intensities and object phases are shown in Fig. 6. For this gold test pattern, the accurate complex transmission function is unknown, so that the R factor is difficult to calculate. The advantage of estimating SNR from correlation coefficient is that the information about the original image is not required. Any pair of the 10 reconstructions with different random starts can be used to estimate a SNR value. The obtained 45 values are then averaged. Fig. 6 (b) and (d) indicate that both concentric and Fermat spiral scan patterns give high quality images for high overlapping ratios. The SNR for Fermat spiral reconstruction is about 6% higher. For the less overlapping condition (shown in Fig. 6 (f) and (h)), noticeable artifacts start to show in the reconstructed image with the concentric pattern, indicated by red boxes in Fig. 6 (h), while the Fermat spiral pattern is able to reconstruct image with much better quality, which gives about 89% improvement of SNR . The image quality improvement is greater than under the ideal condition in simulation, which implies the Fermat spiral provides higher tolerance on data noise and other measurement imperfections, especially for low overlapping cases.

5. Discussion

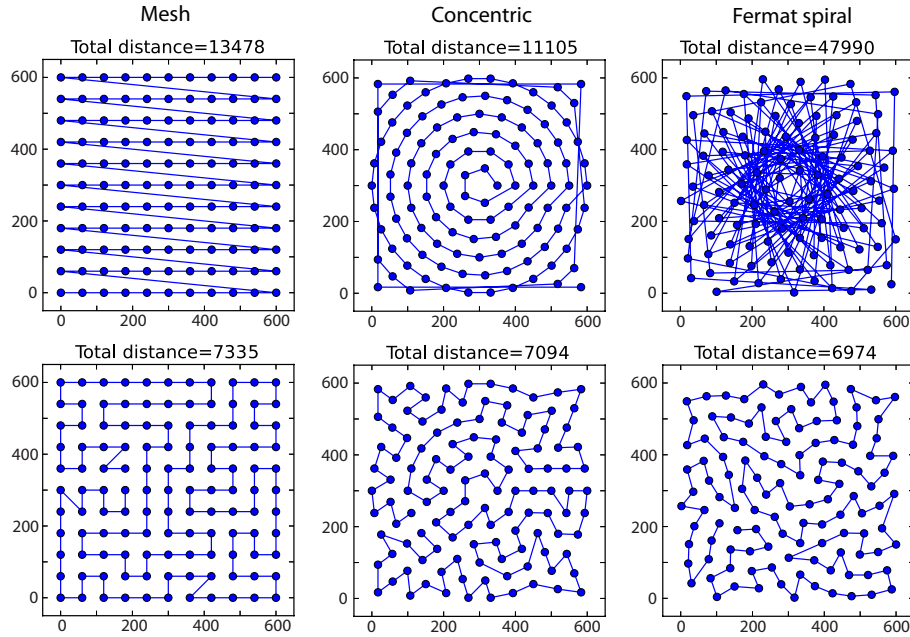


Fig. 7. Top row: the default scan trajectories for mesh, concentric and Fermat spiral patterns. Bottom row: the scan trajectories sorted by minimizing the total movement distances using the Metropolis algorithm.

The Fermat spiral pattern defined by Eq. 1 naturally grows in an order from the center to edges in the same manner as the concentric pattern, as shown in the top row of Fig. 7. This allows rapid reconstructions using continuous subsets of the full ptychography dataset to visualize the central part of the object, which is most interesting region for most cases. However, because 2 adjacent points in the Fermat spiral pattern are separated by 137.508° , which significantly increases the distance for motor motion. Fortunately, since high positioning accuracy is preferred, most ptychography measurements are conducted with modern piezo scanners, where the movement is completed almost instantly. For other cases, if the motor motion time is not negligible and proportional to the moving distance, the scan trajectory can be optimized to minimize the total movement distance. The bottom row of Fig. 7 shows the scan trajectories that are sorted using the Metropolis algorithm [24, 25]. The sorted Fermat spiral actually gives the shortest total travel distance, which is consistent with its highest overlapping ratio. This effect is also reflected by the smallest scan range covered by the Fermat spiral pattern. The evidence can be found in the second row of Fig. 5, where the Fermat spiral gives the largest number of zero-value pixels.

6. Conclusion

The Fermat spiral defines a uniformly distributed pattern with no symmetry, which fulfills the requirements for an ideal ptychography scan trajectory. Numerical simulation shows that using Fermat spiral as a ptychography scan pattern increases image quality by at least 4%, when compared with the concentric pattern. The performance improvement arises from more uniform coverage and slightly higher overlapping ratio. A more significant performance enhancement was observed from experimental data with noise and other measurement imperfections, especially for low overlapping conditions.

Acknowledgments

Work at Brookhaven was supported by the Department of Energy, Office of Basic Energy Sciences under contract DE-AC-02-98CH10886. I.K.R. is supported by the ERC “nanosculpture” advanced grant 227711. The measurements were carried out at APS beamline 34-ID-C, built with US National Science Foundation grant DMR-9724294 and operated by the US Department of Energy, Office of Basic Energy Sciences, under contract no. DE-AC0206CH11357.